DE GRUYTER DOI 10.1515/jnet-2014-0026 — J. Non-Equilib. Thermodyn. 2014; 39 (4):231–248

Research Article

Hugo A. Castillo, Jorge Castillo Tejas, Juan Paulo García-Sandoval, Oscar Matus, Fernando Bautista, Jorge E. Puig and Octavio Manero

Derivation of the mechanical and thermodynamic potentials from the generalized BMP model under shear-banding flow

Abstract: In this work, we demonstrate that the thermodynamic potential calculated from the steady-state flow curve using the definition of free energy from irreversible thermodynamics, and the mechanical potential derived from the generalized BMP constitutive equation provide the same information in the unstable and metastable regions of the flow curve. The contribution of normal stresses in both potentials as well as its weight on the position of the stress plateau are explicitly exposed. The plateau stress is univocally defined by the location of the critical shear rates corresponding to the minima in the potential. This demonstration is carried out using experimental data of wormlike micellar solutions for various concentrations and temperatures, including regions close to the non-equilibrium critical point. A method to accurately determine the non-equilibrium critical point (or the critical temperature) in a direct form is provided here. Bifurcation points are defined, notably one located at the high shear-rate branch of the flow curve separating the regions of one real solution and three real solutions. The first normal stress difference exhibits three real solutions as sources of elastic instabilities in the high shear band. The contribution of the second normal-stress difference in both the mechanical and thermodynamic potentials is clearly exposed. These results demonstrate that the non-equilibrium phase transition and the mechanical instability as sources of the banded flow are essentially two manifestations of the same reality.

Keywords: BMP model, mechanical potential, thermodynamic potential, shear-banding, complex fluids

---

Hugo A. Castillo, Octavio Manero: Instituto de Investigaciones en Materiales, Universidad Nacional Autónoma de México, A.P. 70-360, México D.F., 04510, Mexico, e-mail: hacs90@hotmail.com, manero@unam.mx
Jorge Castillo Tejas: Facultad de Ciencias Básicas, Ingeniería y Tecnología, Universidad Autónoma de Tlaxcala, Calzada Apizaquito S/N, Apizaco, Tlaxcala, 90300, Mexico, e-mail: j_castillo_tejas@hotmail.com
Juan Paulo García-Sandoval: Departamentos de Física e Ingeniería Química, Universidad de Guadalajara, Blvd. Marcelino García Barragán 1451, Guadalajara, Jalisco 44430, Mexico, e-mail: paulo.garcia@cucei.udg.mx. http://orcid.org/0000-0001-6889-0140
Oscar Matus, Fernando Bautista, Jorge E. Puig: Departamentos de Física e Ingeniería Química, Universidad de Guadalajara, Blvd. Marcelino García Barragán 1451, Guadalajara, Jalisco 44430, Mexico, e-mail: oscarmmatus@gmail.com, ferbautistay@yahoo.com, puig_jorge@hotmail.com

Communicated by: David Jou

1 Introduction

There is increasing evidence, both numerical and experimental, of the analogy between mechanical instability and non-equilibrium thermodynamic phase transition in inhomogeneous flows of wormlike micelles. Spatially inhomogeneous flow patterns, namely shear bands, resemble the coexistence of two “phases”, the highly oriented and the non-oriented flow regions. In this regard, the similarities between the shear-banding transition and a thermodynamic phase transitions have been a provocative and a standing issue [1–8].

The shear-induced phase transition mechanism is supported by several arguments, namely: a reversible shear-induced structural or non-equilibrium phase transition; the existence of the plateau stress which is unique, robust and independent of flow history; the long stress oscillations in transient flows that reflect the kinetics of nucleation and growth of a second phase, similar to that observed in equilibrium first order transitions; and the similarities found between the master flow-phase diagram constructed by temperature-concentration superposition and the equilibrium liquid-vapor phase diagrams [9, 10]. In addition, the lever rule derived from the Maxwell construction by equating the chemical potentials under gas-liquid equilibrium is analogous to that derived from the spatial proportion of bands, in which the applied shear rate and the binodals (extremes of the plateau), corresponding to the two critical shear rates, determine this band proportion [9, 11].

The appearance of the stress plateau is similar to the behavior of thermodynamic first-order phase transition. Experimental observations and computer simulations have suggested this analogy. To describe such behavior theoretically, some constitutive models predict a cubic flow curve that strongly reflects the pressure-volume plot as a function of the temperature predicted by the van der Waals or other cubic equation of state [12, 13]. To elaborate more on the analogy, the constitutive flow curve exhibits a bands-coexistence envelope, a region of instability akin to the spinodal region in pressure-volume plots, and two metastable regions that collapse into a critical or inflection point. As experimentally observed, when the temperature or surfactant concentration is increased, the shear-banding region diminishes, and it vanishes at a critical temperature or surfactant concentration [14, 15].

To describe the spinodal and coexistence lines out of equilibrium, thermodynamic models based on non-equilibrium chemical potentials that include shear effects have been forwarded [16, 17]. The unique stress selection is based on the equality of the generalized Gibbs free energy of the stable flow branches. The criterion on the equality of the extended free energy not only selects the stress plateau, but it also is closely related to the stability analysis [18]. Stable and metastable regions of the flow curve are then coupled to the minima or maxima of the free energy along the constitutive curve [19]. A plot of the normalized stress and the shear rate for various temperatures maintaining the concentration constant reveals that experimental data collapse in the regions of homogeneous flow at low and high shear rates, but describe several flat lines in the region of intermediate stress (the stress plateau) depending on the temperature. As the temperature increases, the width of the stress plateau (located between the critical shear rates $\dot{\gamma}_{c1}$ and $\dot{\gamma}_{c2}$) diminishes and ends at the non-equilibrium critical point where for higher temperatures, a monotonic increase instead of a plateau is observed. The dissipated energy (or extended Gibbs free energy) depicts a single minimum in the low and high shear rate Newtonian regions (homogeneous flow) and two minima in the multi-valued stress versus shear rate region (non-homogeneous flow) [19]. The multi-valued region itself contains three sub-regions: one unstable or shear-banding region, corresponding to the negative slope of the cubic flow curve, and two metastable sub-regions, where the slope is positive. The first metastable sub-region is located between the first Newtonian region and the top jumping stress (maximum of the flow curve) and the second metastable sub-region is located between the minimum of the flow curve and the second Newtonian region (see Figure 1). It turns out that in the metastable regions the free energy exhibits two minima, one of them is deeper than the other, while in the shear-banding region both minima have the same depth. The later scenario determines the location of the stress plateau and of the critical shear rates for shear-banding, $\dot{\gamma}_{c1}$ and $\dot{\gamma}_{c2}$.

From the extended free energy it is possible for the particular case of shear flow, to relate the free energy to the two important conjugate variables: the stress and shear rate [20]. Likewise, the free energy itself under isobaric and isothermal conditions can be related to the dissipation arising in a flowing micellar solution. The equal area construction in this case represents the dissipated energy above and below the plateau stress, which reflects the equal minima of the thermodynamic potential [19]. Thus, the stress plateau is defined as the set of points along which the extended Gibbs free energy exhibits two equal minima when plotted against the shear rate.

In this work, we derive the mechanical potential from the constitutive equations of the generalized BMP model [18], which includes normal stresses within a tensorial formulation, and the thermodynamic potential from the same model, using the known relationships derived from irreversible thermodynamics.

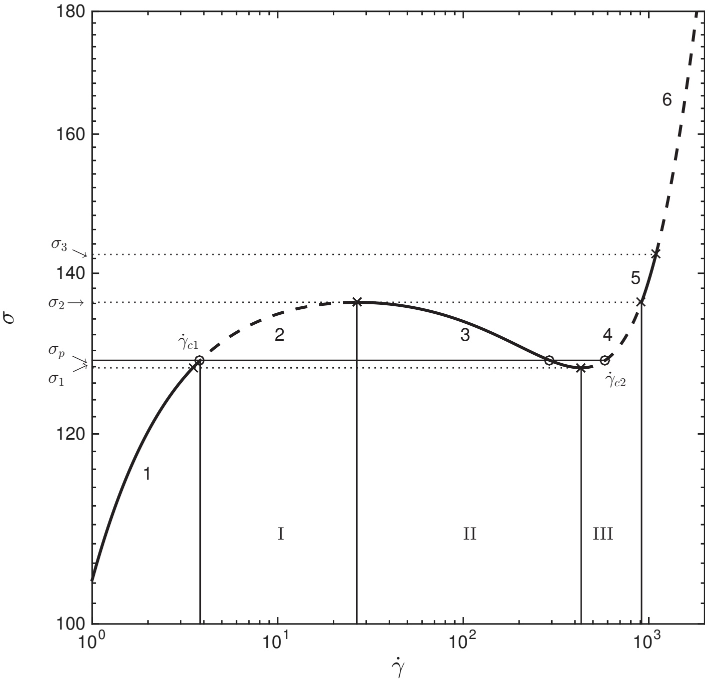

Figure 1. Stress versus shear rate for a 20 wt.% CTAT solution at 25 °C ($\varphi_0 = 4.2 \times 10^{-3}$, $\varphi_\infty = 12$, $k\lambda = 4.3 \times 10^{-6}$, $\vartheta = 1.5 \times 10^{-3}$). Regions I, II and III correspond to the first metastable, unstable and second metastable regions, respectively. σ_1, σ_2 and σ_3 are the stresses located at the bifurcation points, and σ_P is the plateau stress. Sections 1–6 correspond to homogeneous flow (1 and 5), metastable flow (2 and 4), unstable flow (3) and multivalued region at high shear rates (6). $\dot\gamma_{c1}$ and $\dot\gamma_{c2}$ correspond to the critical shear rates (extremes of the plateau stress or binodals).

2 The generalized BMP model

We start with the following constitutive equations comprising the set of the generalized BMP model equations [18]:

$$\frac{d\phi}{dt} = \frac{1}{\lambda}(1-\phi) + k_0\big(1+\vartheta(II_D)\big)(\phi_\infty - \phi)\underline{\underline{\sigma}} : \underline{\underline{D}} + \frac{1}{\rho}\nabla \cdot \bar{J}, \tag{2.1}$$

$$\phi\bar{J} + \tau_1\overset{\nabla}{\bar{J}} = -\mathcal{D}\nabla c - \rho\mathcal{D}'\nabla\phi + \tau_\sigma\nabla \cdot \underline{\underline{\sigma}}, \tag{2.2}$$

$$\phi\underline{\underline{\sigma}} + \tau_\sigma\overset{\nabla}{\underline{\underline{\sigma}}} = 2\eta_0\underline{\underline{D}} + \Psi_2\underline{\underline{D}} \cdot \underline{\underline{D}} + \mathcal{D}(\nabla\bar{J})^s, \tag{2.3}$$

where $(\nabla\bar{J})^s$ stands for the symmetric part of $\mathrm{grad}(\bar{J})$. The upper-convected derivatives of the mass flux vector and of the total stress tensor σ are defined, respectively, as

$$\overset{\nabla}{\bar{J}} = \frac{d\bar{J}}{dt} - L \cdot \bar{J},$$

$$\overset{\nabla}{\underline{\underline{\sigma}}} = \frac{d\underline{\underline{\sigma}}}{dt} - (L \cdot \underline{\underline{\sigma}} + \underline{\underline{\sigma}} \cdot L^T).$$

Here L is the velocity gradient tensor, D is the symmetric part of the rate-of-strain tensor, and II_D is its second invariant. Moreover, $\phi = \varphi/\varphi_0$, where φ is the fluidity (inverse of the shear viscosity η) and $\varphi_0 \equiv \eta_0^{-1}$ is the fluidity at vanishing strain rates, ϕ_∞ is the fluidity at high strain rates, λ is a structure relaxation time, k_0 can be interpreted as a kinetic parameter for structure breaking, τ_1 is a relaxation time for the mass flux, τ_σ is the stress relaxation time, $\mathcal{D}$ is the Fickean diffusion coefficient, $\mathcal{D}'$ is the structure diffusion coefficient, Ψ_2 is the second normal stress coefficient, c is the local equilibrium concentration, and ϑ is the shear-banding intensity parameter.

Equations (2.1)–(2.3) together with the conservation equations represent a closed set of time evolution equations for all the independent variables chosen to describe the behavior of complex fluids. Conservation of mass, concentration, and momentum reads

$$\nabla \cdot v = 0, \tag{2.4}$$

$$\frac{\partial c}{\partial t} = -\nabla \cdot J, \tag{2.5}$$

$$\rho \frac{\partial \underline{v}}{\partial t} = -\nabla \cdot \underline{\underline{\sigma}} + \eta_s \nabla^2 \underline{v}. \tag{2.6}$$

For simple-shear (where x is the direction of the macroscopic flow velocity, y the direction of the velocity gradient, and z the vorticity direction) we assume small inertia and that the mass flux relaxation time is negligible small compared to the stress relaxation time, i.e., $1/G_0\varphi \gg \tau_1$. The set of resulting equations is

$$\frac{\partial \phi}{\partial t} = \frac{1}{\lambda}(1-\phi) + k_0(1+\vartheta\dot{\gamma})(\phi_\infty - \phi)\sigma_{xy}\dot{\gamma} - \mathcal{D}'\left[\frac{\partial}{\partial y}\left(\frac{1}{\phi}\frac{\partial \phi}{\partial y}\right)\right] - \frac{\mathcal{D}}{\rho}\left[\frac{\partial}{\partial y}\left(\frac{1}{\phi}\frac{\partial c}{\partial y}\right)\right], \tag{2.7}$$

$$\phi\sigma_{xy} + \tau_\sigma\left[\frac{\partial \sigma_{xy}}{\partial t}\right] = \eta_0\dot{\gamma} + \dot{\gamma}\tau_\sigma N_2 + \frac{\mathcal{D}\tau_\sigma}{2}\frac{\partial}{\partial y}\left[\frac{1}{\phi}\frac{\partial \sigma_{xy}}{\partial y}\right], \tag{2.8}$$

$$\phi N_1 + \tau_\sigma\left[\frac{\partial N_1}{\partial t} - 2\dot{\gamma}\sigma_{xy}\right] = -\Psi_2\dot{\gamma}^2 + \rho\mathcal{D}\mathcal{D}'\frac{\partial}{\partial y}\left[\frac{1}{\phi}\frac{\partial \phi}{\partial y}\right] + \mathcal{D}^2\left[\frac{\partial}{\partial y}\left(\frac{1}{\phi}\frac{\partial c}{\partial y}\right)\right], \tag{2.9}$$

$$\phi N_2 + \tau_\sigma\left[\frac{\partial N_2}{\partial t}\right] = \Psi_2\dot{\gamma}^2 - \rho\mathcal{D}\mathcal{D}'\frac{\partial}{\partial y}\left[\frac{1}{\phi}\frac{\partial \phi}{\partial y}\right] - \mathcal{D}^2\left[\frac{\partial}{\partial y}\left(\frac{1}{\phi}\frac{\partial c}{\partial y}\right)\right], \tag{2.10}$$

where $N_1 = \sigma_{xx} - \sigma_{yy}$ and $N_2 = \sigma_{yy} - \sigma_{zz}$. Under steady-state, Eqs. (2.5)–(2.10) become

$$0 = \frac{1}{\lambda}(1-\phi) + k_0(1+\vartheta\dot{\gamma})(\phi_\infty - \phi)\sigma_{xy}\dot{\gamma}, \tag{2.11}$$

$$\phi\sigma_{xy} = \eta_0\dot{\gamma} + \dot{\gamma}\tau_\sigma N_2, \tag{2.12}$$

$$\phi N_1 = (2\tau_\sigma\sigma_{xy} - \Psi_2\dot{\gamma})\dot{\gamma}, \tag{2.13}$$

$$\phi N_2 = \Psi_2\dot{\gamma}^2. \tag{2.14}$$

Integration of Eq. (2.6) under steady-state gives the total stress, independent of y:

$$\underline{\underline{\sigma}} + \eta_s \nabla \underline{v} = \text{const.} = \underline{\underline{\sigma}}^*.$$

Substituting Eq. (2.14) into Eqs. (2.11) and (2.12) gives

$$\phi^3 + a'\phi^2 + b'\phi - c' = 0, \tag{2.15}$$

$$a' = k_0\lambda(1+\vartheta\dot{\gamma})\eta_0\dot{\gamma}^2 - 1, \tag{2.16}$$

$$b' = k_0\lambda(1+\vartheta\dot{\gamma})\dot{\gamma}^2[\Psi_2\tau_\sigma\dot{\gamma}^2 - \eta_0\phi_\infty], \tag{2.17}$$

$$c' = k_0\lambda(1+\vartheta\dot{\gamma})\Psi_2\dot{\gamma}^4\phi_\infty\tau_\sigma. \tag{2.18}$$

For an imposed shear rate, Eq. (2.15) renders the three roots for the fluidity, from which the stress can be calculated. However, it is difficult to find the multivalued region for a given stress. It is then necessary to modify the equations for a controlled stress scheme, i.e.,

$$\phi^3 - a\phi^2 + b\phi - c = 0, \tag{2.19}$$

$$a = \phi_\infty - 1/\beta\vartheta, \tag{2.20}$$

$$b = (k_0\lambda\vartheta\sigma_{xy}\beta^2)^{-1} - \phi_\infty/\beta\vartheta, \tag{2.21}$$

$$c = (k_0\lambda\vartheta\sigma_{xy}\beta^2)^{-1}, \tag{2.22}$$

$$\beta = \sigma_{xy}/(\eta_0 + \tau_\sigma N_2). \tag{2.23}$$

Here N_2 will be considered as a small perturbation. For a given input stress, and knowing the solutions of Eqs. (2.15)–(2.18), Eq. (2.12) gives new values of the shear rate. Calculation of Eqs. (2.19)–(2.23) provides the roots of the fluidity, which must be the same roots found using the exact Eq. (2.15). The procedure is repeated for various values of the second normal stress coefficient as follows:

$$\Psi_2 = N_2/\dot{\gamma}^2 = \Psi_1 x,$$

where $x = 10^{-1}, 10^{-2}, 10^{-3}, 10^{-4}$.

3 Derivation of the mechanical potential

The three roots of Eq. (2.19) are themselves functions of the applied stress. The first root covers the region of positive slope from low values of the stress up to the top-jumping stress or first maximum in Figure 1 (regions 1 and 2). The second root goes from the minimum of the curve to high stress values in the positive slope region (regions 4 to 6 of Figure 1) and the third root goes along the negative slope region (from the top-jumping stress down to the minimum in the flow curve, i.e., region 3 of Figure 1).

The regimes corresponding to a single root and three real roots are separated in the space of parameters u and v by the cubic equation, $4u^3 + 27v^2 = 0$, where u and v are defined in Eqs. (3.2) and (3.3). This cubic equation sets the loci of the bifurcation points along the flow curve, inasmuch as it sets the limits of the single-valued regions and multiple-valued regions. The first and second bifurcation points are located at the crossing points of the flow curve and the dashed line in Figure 1, which correspond to the applied stress σ_1 and σ_2, respectively. As observed, these are the bounds of the multiple-valued region.

There are six different sections of the flow curve depending on the nature of the roots. The first section (1) covers the homogeneous low-stress region up to the first bifurcation point, corresponding to one real and two imaginary roots of Eq. (2.19). Sections 2, 3 and 4 have three real roots; section 2 goes from the first bifurcation up to the top jumping stress, section 3 covers the negative slope, and section 4 goes from the minimum up to the second bifurcation point. As indicated in Figure 1, sections 2 and 4 are the meta-stable sub-regions and section 3 is unstable or the shear-banding region. The limits of section 3 (maximum and minimum) correspond to two points belonging to the spinodal line. Finally, section 5 has one real root and two imaginary roots, as a counterpart similar to section 1. An unexpected result is the existence of a third bifurcation point in the high-stress region of the flow curve. In fact, section 6 again has three real roots, but two of them are negative. Therefore, although sections 5 and 6 are homogeneous flow regions, we may expect differences in the flow and fluid behavior.

Eq. (2.19) can be expressed as follows:

$$0 = \phi'^3 + u\phi' + v, \tag{3.1}$$

where $\phi' = \phi - a/3$, and

$$u = b - a^2/3, \tag{3.2}$$

$$v = ab/3 - 2a^3/27 - c, \tag{3.3}$$

which can in turn be written in terms of the mechanical potential V as

$$0 = \frac{dV}{d\phi'},$$

where

$$V = \phi'^4/4 + u\phi'^2/2 + v\phi'. \tag{3.4}$$

The following expressions provide an insight into the solutions of Eq. (3.1). Defining

$$R = (u/3)^3 + (v/2)^2, \tag{3.5}$$

$$A = (-v/2 + \sqrt{R})^{1/3}, \tag{3.6}$$

$$B = (-v/2 - \sqrt{R})^{1/3}, \tag{3.7}$$

the solutions of Eq. (3.1) are

$$\phi_1' = A + B, \tag{3.8}$$

$$\phi_2' = -1/2(A + B) + \sqrt{3}/2(A - B)i, \tag{3.9}$$

$$\phi_3' = -1/2(A + B) - \sqrt{3}/2(A - B)i. \tag{3.10}$$

As observed, these solutions depend on the parameter R and v. As explained later, the zeros of these parameters define the loci of the plateau and bifurcation lines. Four cases can be analyzed.

3.1 Case $R > 0$

In this case A and B are real and so the first solution of Eq. (3.1) is real. The other two are complex conjugates. Given applied stresses corresponding to regions 1 and 5 in Figure 1, u, v and hence R, A and B can be calculated. Then Eq. (3.1) gives the value of the modified fluidity in these regions.

3.2 Case $R = 0$

In this case, Eqs. (3.5)–(3.10) give three real solutions, two of them are equal. These are

$$\phi_1' = \pm 2\sqrt{|u|/3}, \tag{3.11}$$

$$\phi_2' = \phi_3 = \mp\sqrt{|u|/3}. \tag{3.12}$$

The stresses corresponding to $R = 0$ are shown as dashed lines in Figure 1. The smallest one intersects the first bifurcation point and the minimum of the flow curve. These intersections are located at the positions given by Eqs. (3.11) (negative root) and (3.12) (positive root), respectively. The intermediate stress intersects the flow curve in two points: the maximum (Eq. (3.12), negative root) and the second bifurcation point (Eq. (3.11), positive root). In fact, the first derivative of Eq. (3.1) gives the position of the maximum and the minimum of the flow curve (Eq. (3.12)). Finally, the largest stress for $R = 0$ corresponds to the third bifurcation point located in the high shear rate branch (Eq. (3.11)), dividing regions 5 and 6.

3.3 Case $R < 0$

In this case, Eqs. (3.8)–(3.10) render three real solutions corresponding to regions 2, 3 and 4 in Figure 1, respectively. These are

$$\phi_1' = 2\sqrt{|u|/3}\cos(\theta/3), \tag{3.13}$$

$$\phi_2' = -2\sqrt{|u|/3}\cos((\theta + \pi)/3), \tag{3.14}$$

$$\phi_3' = -2\sqrt{|u|/3}\cos((\theta - \pi)/3), \tag{3.15}$$

$$\theta = \cos^{-1}((-v/2)/(u/3)^{3/2}). \tag{3.16}$$

For stresses between those corresponding to the first and second bifurcation points, three points of intersection are located in the two metastable flow regions (2 and 4) and one unstable flow region (3). Eqs. (3.13) and (3.14) meet at the maximum and Eqs. (3.14) and (3.15) meet at the minimum of the flow curve.

3.4 Case $v = 0$

This case is associated to the location of the plateau stress. In fact, Eq. (3.1) or Eqs. (3.13)–(3.16) give the following solutions:

$$\phi_1' = 0, \quad \phi_2' = -\sqrt{|u|}, \quad \phi_3' = \sqrt{|u|}. \tag{3.17}$$

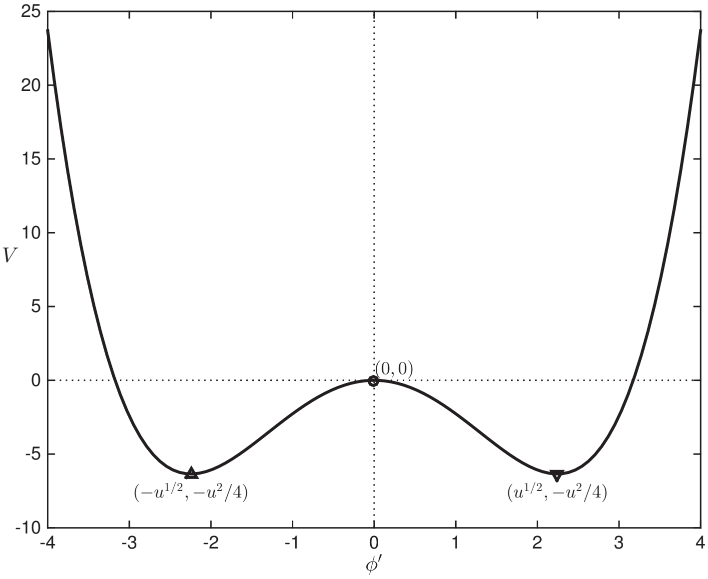

Figure 2. Mechanical potential as a function of modified fluidity for a 20 wt.% CTAT solution at 25 °C. The three roots of the multivalued region are indicated, two at the minima and one at the maximum. The depth of the potential and the separation of the two minima are functions of u as indicated.

T	φ_0	φ_∞	$k\lambda$	ϑ	G_0
30 °C	0.01	7	2×10^{-4}	0.015	54.5
38 °C	0.069	10	5×10^{-5}	0.012	57.5
40 °C	0.105	11	3×10^{-5}	0.01	64
45 °C	0.24	16	1×10^{-5}	0.007	68
50 °C	0.45	17	9×10^{-6}	0.004	68
55 °C	1.3	19	7×10^{-6}	0.001	69

Table 1. Parameter values used for the BMP model (5 wt.% CTAT solutions).

The first solution corresponds to the inflection point of the flow curve, coinciding with the null second derivative of Eq. (3.1). As shown later, the plateau stress has two main properties: the areas above and below the plateau stress are equal, and the potential associated to this stress has equal heights. In fact, Eq. (3.4) gives, for $v = 0$,

$$V = \phi'^4/4 + u\phi'^2/2. \tag{3.18}$$

Substituting Eq. (3.17) into Eq. (3.18) gives

$$V = -(u)^2/4.$$

This means that the potential has two minima with equal magnitude symmetrically separated from the origin (see Figure 2), i.e., the potential, Eq. (3.18), describes two minima and one maximum corresponding to the three roots (Eqs. (3.17)). The plot of u and v as a function of the stress reveals that the crossing at $v = 0$ gives the value of the plateau stress, corresponding to a negative value for u. This value for u sets the symmetric position and magnitude of the minima of the mechanical potential.

When the two minima have equal heights, they are located at the critical fluidities ϕ_{c1} and ϕ_{c2}. Furthermore, the ratio of the critical shear rates to critical fluidities is precisely the plateau stress:

$$\sigma_p = (\dot{\gamma}_c/\phi_c)_1 = (\dot{\gamma}_c/\phi_c)_2.$$

The influence of the second normal stress difference on the position of the plateau stress can be analyzed, and the results are exposed in Figure 3. In Figure 3a, data for a 5 wt.% CTAT solution at 40 °C (see Table 1) is used. The variable u is plotted versus the second normal-stress coefficient. It is observed that for values of the coefficient larger than 0.01, the plateau stress is modified by Ψ_2, and no modification is observed below this value. This is clearly seen in Figure 3b, where the plateau stress value is plotted versus the second normal-stress coefficient.

In Figure 4, the mechanical potential for this system is plotted against the modified fluidity. For this value of the second normal-stress coefficient (0.0028 units), equal minima in the potential lead to the determination of the position of the stress plateau. In Figure 5, the normal stresses are plotted versus the shear rate. At high shear rates, the magnitude difference between N_1 and N_2 is around two decades. In view of the experimental uncertainties to determine the value of the second normal-stress difference, this is a reasonable prediction.

Changes in the flow curves arising from increasing the value of the second normal-stress coefficient are depicted in Figure 6. In Figure 6a, a small coefficient gives the same results compared to $\Psi_2 = 0$, but a substantial change in the flow curve at high shear rates is observed when Ψ_2 is increased. Similarly, the position of the third bifurcation point at high shear rates, represented by the value of the shear rate, does not change substantially for the second normal stress coefficients smaller than 0.0028, as observed in Figure 6b. Notwithstanding, the same plateau stress is predicted.

4 Behavior near the non-equilibrium critical point

As the non-equilibrium critical point (NECP) is approached, the span of the plateau gradually diminishes and the two critical shear rates merge into a single one. This leads to the situation where the minima of the potential in Figure 2 approach each other while their magnitude decreases. In fact, as the NECP is approached, u tends to zero. Thus, the conditions of the location of the NECP are $u = 0$ and $v = 0$. These conditions are fulfilled for a pair of critical values of the plateau stress and shear-banding intensity parameter (σ_{Pc} and ϑ_c).

Predictions for the 5 wt.% solution of CTAT in water at several temperatures are provided in Figure 7, where the normalized stress is plotted against the normalized shear rate. The value of each model parameter corresponding to a given temperature describing the experimental were taken from Rehage and Hoffmann [2].

To interpolate and find the precise location of the NECP, each parameter was plotted as a function of the temperature. At a given temperature, the plateau stress was found using the condition $v = 0$ (see Figure 8a) and given the value of the plateau stress, u is then calculated for various temperatures. (In Figure 8a we can identify the plateau stress at the critical temperature.)

This procedure gives way to the construction of a plot of u as a function of the temperature (see Figure 8b). As the NECP is approached, the two roots of u tend to zero at the critical temperature, as indicated in Figure 8b. Similarly, the difference in critical shear rates $\Delta\dot{\gamma} = \dot{\gamma}_{c1} - \dot{\gamma}_{c2}$ also tends to zero near the NECP (see Figure 8c).

Figure 8d shows the variation of the shear-banding intensity parameter with temperature, allowing the evaluation of the critical value of the parameter ϑ_c at the critical temperature. For higher temperatures, $\vartheta(T)$ tends to zero, signaling in fact the transition from cubic to quadratic-monotonic behavior of the flow curve.

The characteristic lines in Figure 7 are displayed according to the position at each temperature of the spinodal, coexistence (binodal) and bifurcation lines. They are determined by the conditions set in Eqs. (3.11), (3.12) and (3.17), respectively. In summary, we have the following loci of the characteristic lines with respect to the reference $\phi' = 0$:

$$\phi' = \pm\sqrt{|u|/3} \qquad \text{spinodal line,} \tag{4.1}$$

$$\phi' = \pm\sqrt{|u|} \qquad \text{coexistence line,} \tag{4.2}$$

$$\phi' = \pm 2\sqrt{|u|/3} \qquad \text{bifurcation line.} \tag{4.3}$$

An interesting observation is that the line corresponding to the third bifurcation prevails even beyond the NECP into isotherms with higher temperatures than the critical isotherm. Within the low temperature range, Figure 7 also shows that for temperatures lower than 30 °C the second and third bifurcation lines meet (not shown).

Figure 9 shows the variation of R as a function of the applied stress for the 5 and 20 wt.% CTAT solutions. In Figure 9a, the locations of the bifurcation points correspond to the zeros of the function R, where the value

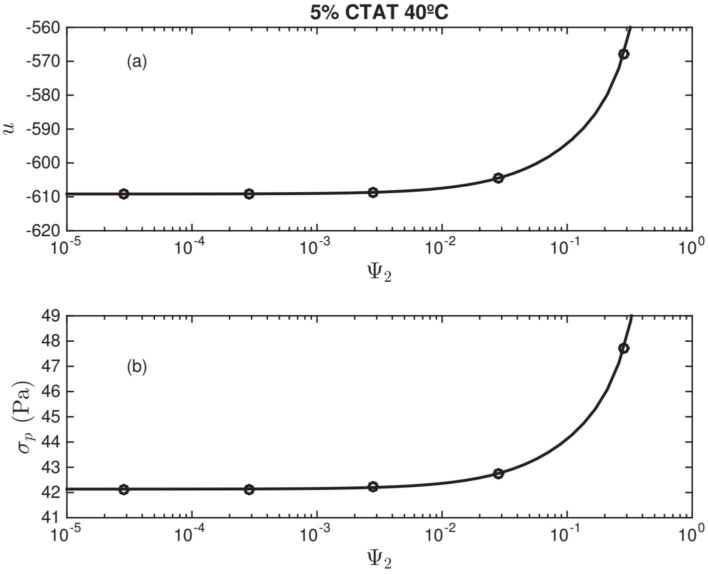

Figure 3. (a) Parameter u defined in Eq. (3.2) as a function of the second normal-stress coefficient Ψ_2. (b) Variation of the plateau stress with Ψ_2.

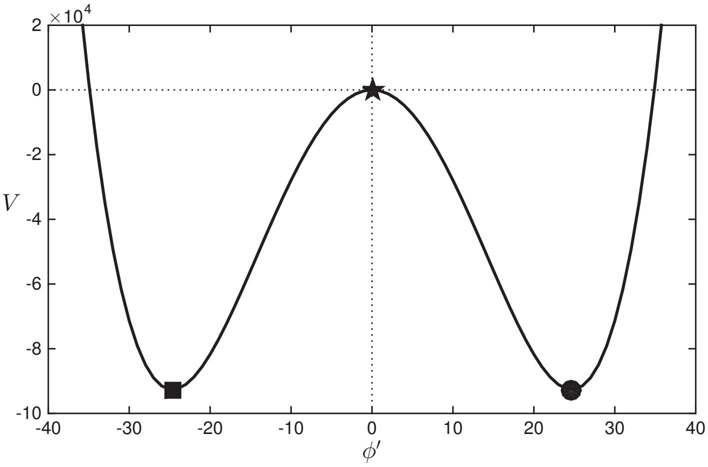

Figure 4. Mechanical potential versus modified fluidity. There is no effect of the second normal stress coefficient on the shape of the potential with $\Psi_2 = 0.0028$.

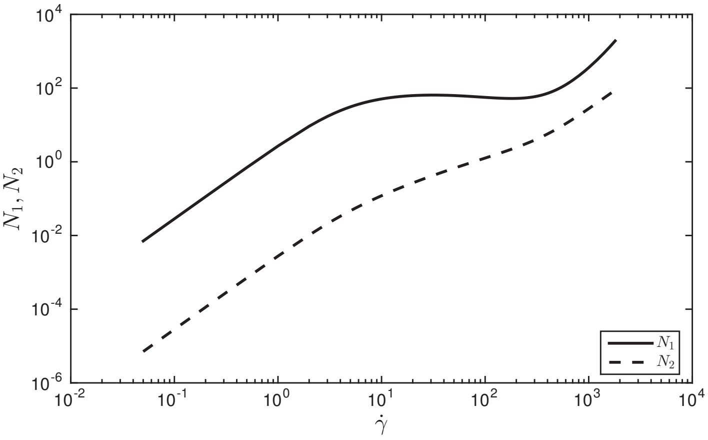

Figure 5. First and second normal stresses as a function of the shear rate.

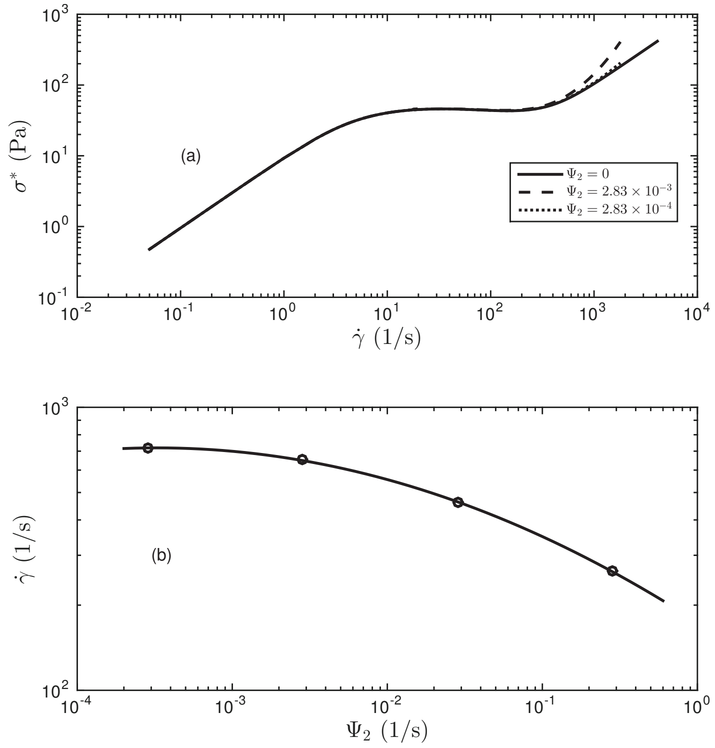

Figure 6. Effect of the second normal stress coefficient on the flow curve (a) and on the third bifurcation point (b).

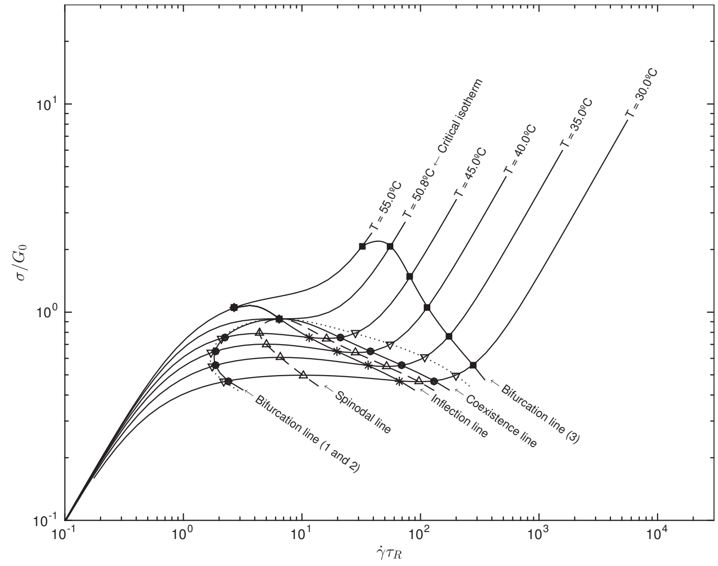

Figure 7. Normalized stress versus normalized shear rate at several temperatures for a 5 wt.% CTAT solution. Spinodal, coexistence and bifurcation lines comply with Eqs.(4.1)–(4.3). They converge to the NECP, except the third bifurcation line.

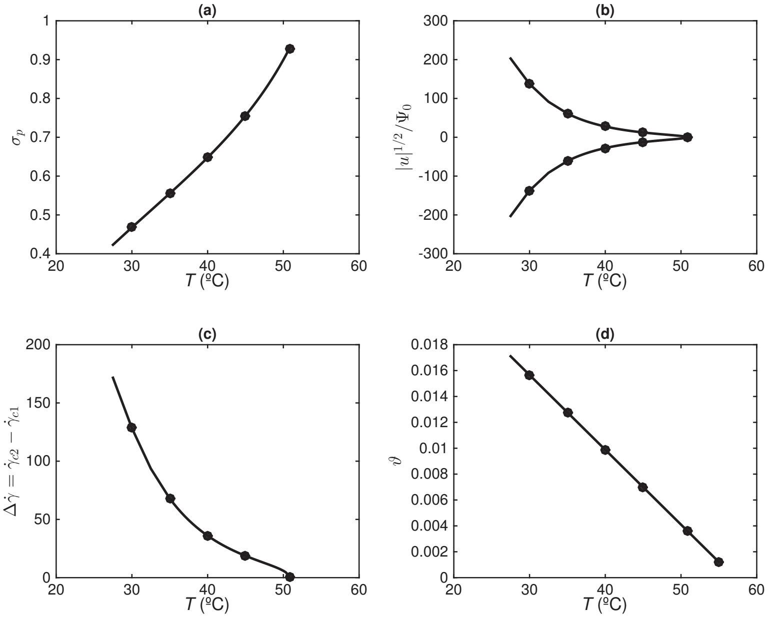

Figure 8. (a) Plateau stress; (b) normalized parameter u (Eq. 3.2); (c) difference between the two critical shear rates; (d) shear-banding intensity parameter, as functions of the temperature.

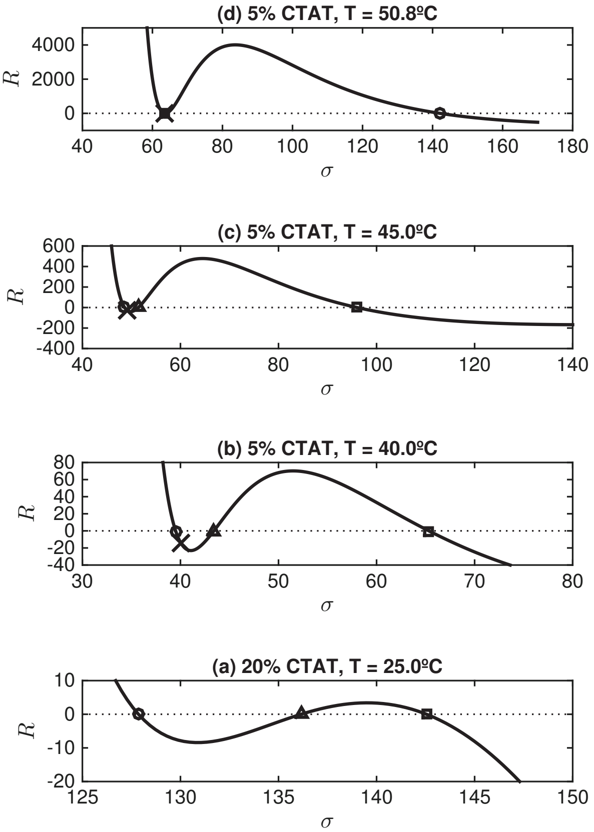

Figure 9. Parameter R (Eq. (3.5)) as a function of the stress for: (a) 20 wt.% CTAT solution at $25\,^{\circ}$C, (b)–(d) 5 wt.% CTAT solution at various temperatures, including the critical temperature. Plots indicate the zeros of the function R. The value corresponding to the plateau stress is also indicated (×).

of the plateau stress is also indicated. The positive values of R correspond to a single homogeneous solution; the negative values correspond to the multivalued region (where the plateau stress is located). The high stress multivalued region corresponds to that when the three roots are real, but only one is positive. In Figures 9b and 9c the plots are for the 5 wt.% solution, where it is clearly shown that the first and second bifurcation points approach each other as the temperature increases. Finally, at the critical temperature (50.8 °C), the first and second bifurcation points merge, leaving the third bifurcation point outside the region of the critical point. The critical isotherm contains a multivalued region at high stresses, as shown in Figure 9d.

The variation of the parameters u and v as a function of the applied stress is shown in Figure 10. Near the critical temperature (50 °C), the plateau set by the condition $v = 0$ corresponds to a negative value of u (see Figure 10a) giving rise to a symmetric position of the potential. At the critical temperature (50.8 °C), the values of u and v are zero as illustrated in Figure 10b. The three roots of Eqs. (3.13)–(3.15) have the value of zero at the critical point according to Eq. (3.1).

A three-dimensional plot of the fluidity as a function of the parameters u and v is shown in Figure 11 for several temperatures. This phase-space projection indicates that at $u = v = 0$ only the data corresponding to $T = 50.8$ °C crosses the line drawn in the 3-D plot. Most points corresponding to the curves of the fluidity at various temperatures lie on the multivalued region near the critical line. The plot gives different symbols to the specific regions of each curve. The projection of the different curves on the u-v plane is displayed in Figure 12 for increasing temperature. The position of the three bifurcation points again is described as the temperature tends to the critical isotherm. The third bifurcation point remains away from the region near the critical point. In fact, as the temperature increases, the first and second bifurcation points approach each other and merge at the NECP, where $u = v = 0$. This is similar to the behavior shown in Figure 9.

5 The thermodynamic potential

According to the Extended Irreversible Thermodynamics of viscoelastic fluids, the extended Gibbs free energy for constant temperature and pressure is given by [16]

$$dG = \frac{v\tau_\sigma\varphi}{2}\underline{\underline{\sigma}} : \underline{\underline{\sigma}}. \tag{5.1}$$

For simple-shear flow, Eq. (5.1) becomes

$$dG = \frac{v\varphi}{2G_0}(2\sigma_{xy}d\sigma_{xy} + \sigma_{xx}d\sigma_{xx} + \sigma_{yy}d\sigma_{yy} + \sigma_{zz}d\sigma_{zz}).$$

From Eqs. (2.11)–(2.14), we obtain

$$dG = \frac{v}{G_0}\left(\sigma_{xy}^2\frac{\phi}{\dot{\gamma}} + 4\sigma_{xy}^2\tau_\sigma^2\frac{\dot{\gamma}}{\phi} + 2\sigma_{xy}\tau_\sigma\Psi_2\frac{\dot{\gamma}^2}{\phi} + 4\sigma_{xy}\tau_\sigma^3\Psi_2\frac{\dot{\gamma}^4}{\phi^3} + \Psi_2^2\frac{\dot{\gamma}^3}{\phi}\right)d\dot{\gamma}. \tag{5.2}$$

The first term is the contribution of the shear stress to the free energy, the second term is that of N_1 and the last three terms represent the contributions of N_2. We then calculate the integral in Eq. (5.2) and find that the thermodynamic potential in fact has two minima and one maximum, and when the minima have the same height, the plateau stress can be obtained (Figure 2). A most interesting result is that the contribution of the normal stresses modifies the shape of the potential but does not change the position of the minima in the thermodynamic potential. Hence, it does not change the position of the binodals or the extremes of the plateau stress (see Figure 13).

Having set the location of the plateau stress, we then calculate the areas above and below the plateau. In fact, by plotting the product of the stress and shear rate (i.e., the dissipation versus shear rate; see Figure 14) the areas become equal, validating the equal-areas criterion derived from the mechanical potential.

It turns out that when comparison is made between the plateau stress calculated using Eq. (5.2) and that calculated from the mechanical potential, a slightly different value is obtained (128.8 versus 130.1 Pa). In Figure 15 we compare the thermodynamic and mechanical potentials for the three cases of the unstable

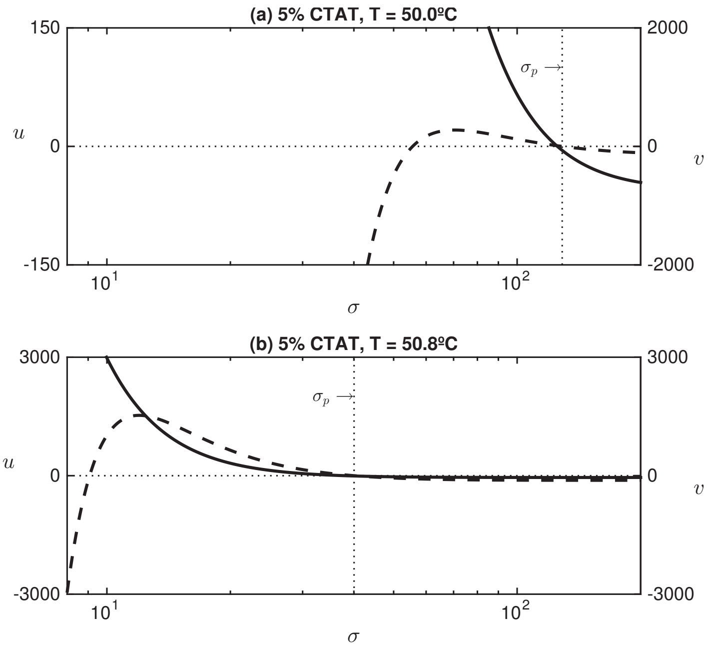

Figure 10. Parameters u and v as functions of the stress for a 5 wt.% CTAT solution. (a) Temperature just below the critical temperature ($50\,^\circ$C); (b) critical temperature ($50.8\,^\circ$C). At the NECP, $v = u = 0$.

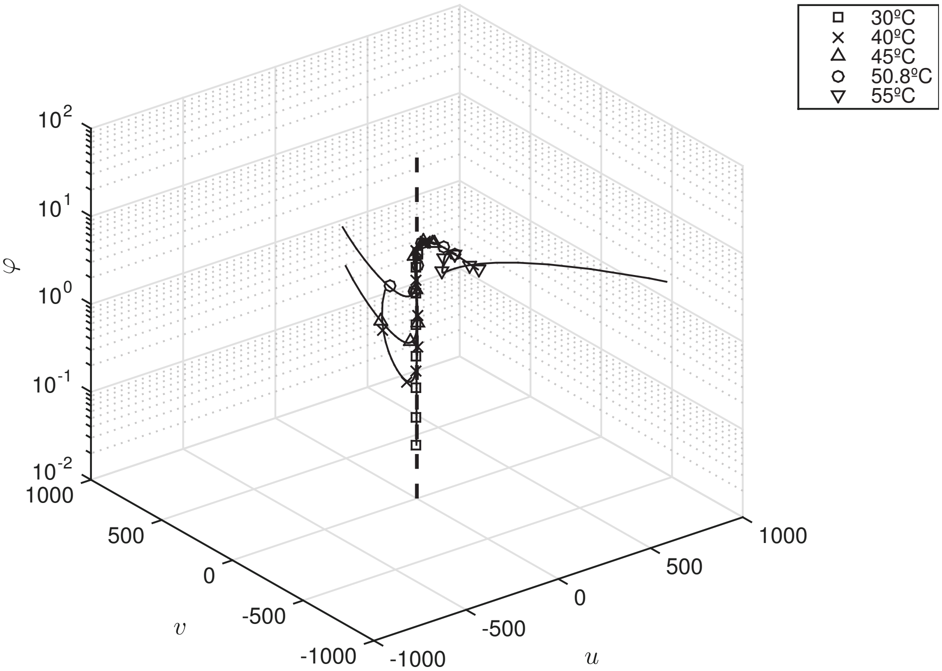

Figure 11. 3-D plot of the fluidity as a function of the parameters v and u, for various temperatures and for a 5 wt.% CTAT solution. Dashed line signals the location of the NECP, and the critical isotherm intersects this line only. $\square$ $30\,^\circ$C, $\times$ $40\,^\circ$C, Δ $45\,^\circ$C, $\circ$ $50.8\,^\circ$C and ∇ $55\,^\circ$C.

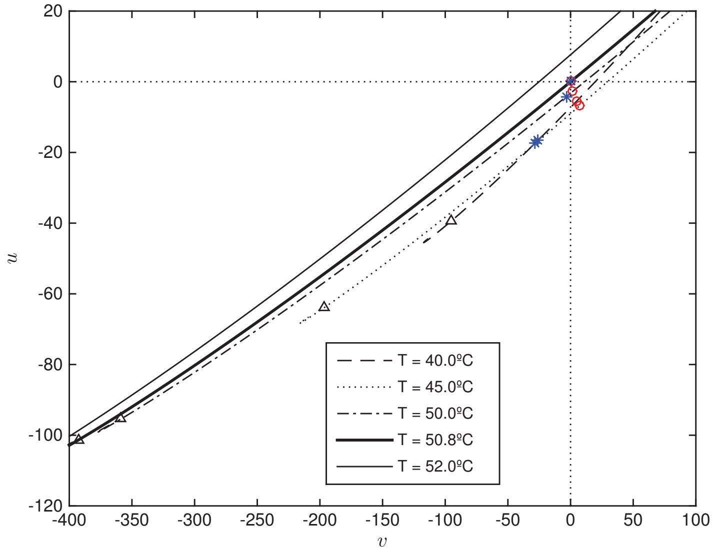

Figure 12. Projection of the lines in Figure 9 on the u-v plane, for several temperatures including the critical temperature. As the temperature increases to values close to the critical temperature, the first and second bifurcation points (circles and stars) approach the $v = u = 0$ limit at the NECP. The third bifurcation point (triangles) remains away from the NECP.

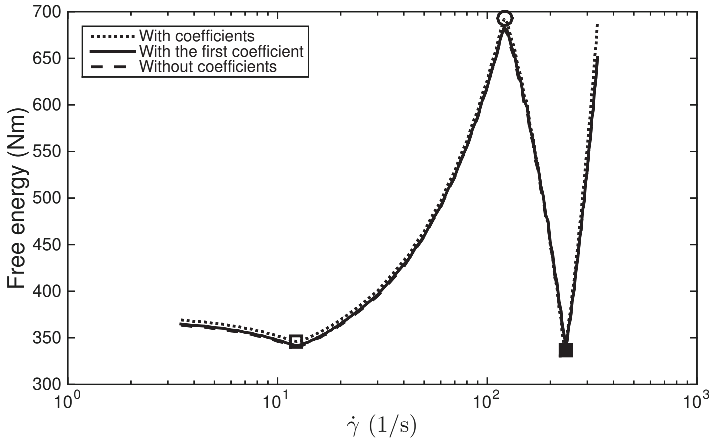

Figure 13. Free energy plotted with shear rate. Contributions from the shear stress, first normal stress difference, and second normal stress differences are indicated.

and two meta-stable regions for a 20 wt.% CTAT solution. For stresses below and above the plateau stress, the two minima have different depths, while at the plateau stress both minima have equal depths. Notice in Figure 15a that the critical shear rates of the thermodynamic and mechanical are slightly shifted, although they have equal minima.

6 Discussion and concluding remarks

In Ref. [19], we have shown that an effective or extended free energy can be constructed from the BMP model using Eq. (5.2). The present formulation is similar to that of the Ginzburg–Landau model for thermodynamic first-order phase transitions, or particularly, it belongs to the class of Cahn–Hilliard dynamics. In a relevant work [21], a mathematical proof of an analogy between the mechanical instability and thermodynamic phase transitions is established for the diffusive Johnson–Segalman model (DJS). Starting from a mechanical constitutive model (DJS), the time-dependent Ginzburg–Landau equation was derived by reducing the degrees

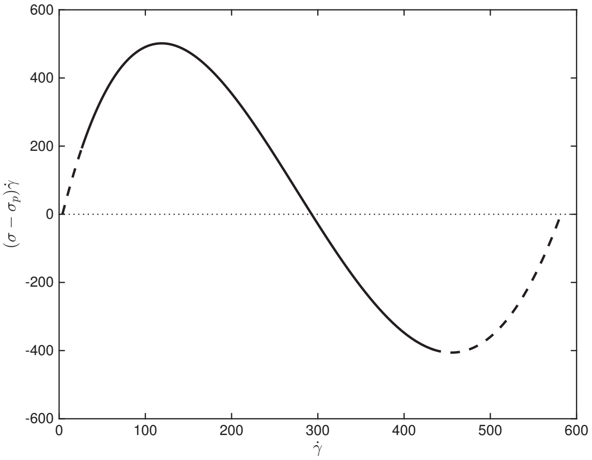

Figure 14. Dissipation above and below the plateau stress as a function of the shear rate for a 20 wt.% CTAT solution at 25 °C. The maximum corresponds to the area above the plateau, and the minimum correspond to the area below the plateau. They have equal values.

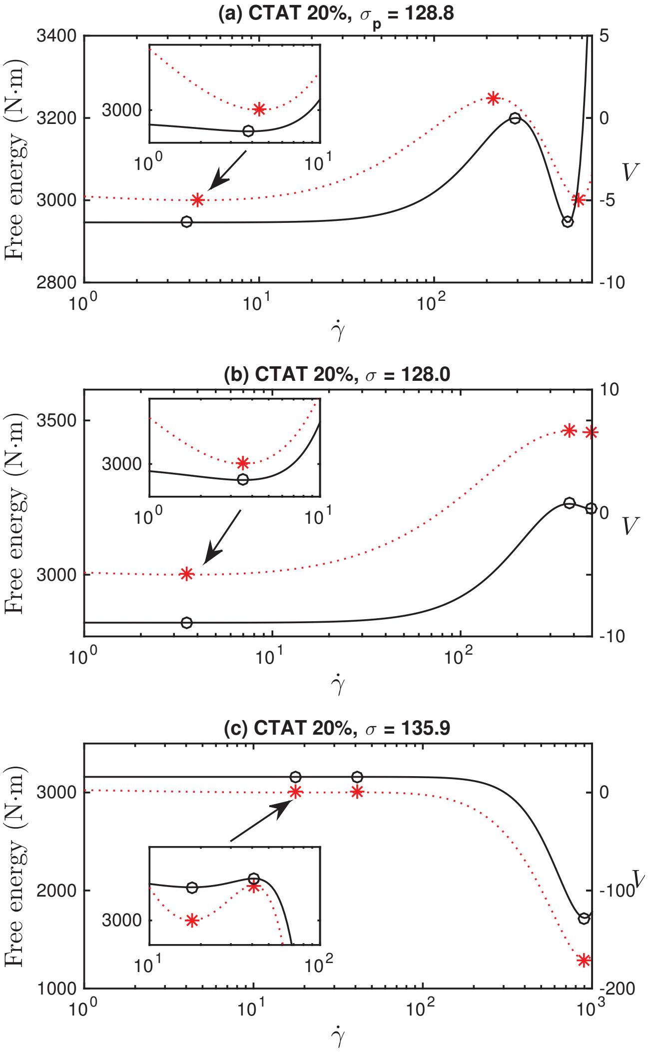

Figure 15. The thermodynamic (free energy) and mechanical potentials as functions of the shear rate for a 20 wt.% CTAT solution at 25 °C. The insets show an amplified view of the minimum at low shear rates. (a) Plateau stress. (b) Stress below the plateau stress. (c) Stress above the plateau stress.

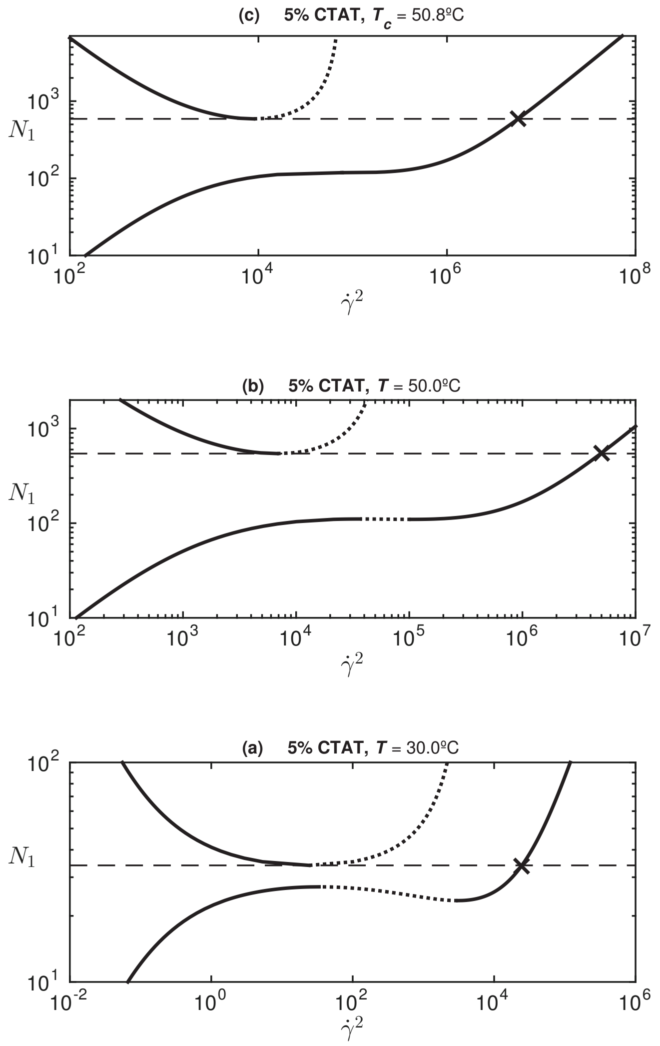

Figure 16. First normal stress difference as a function of shear rate squared, for two temperatures below the critical temperature (a, b) and at the critical temperature (c). Notice that for N_1 larger than its value at the bifurcation line (dashed line), three states are possible, two of them with physical meaning. Similarly, for increasing shear rates, N_1 is double-valued and becomes single valued for shear rates larger than that at the unstable region.

of freedom of the equations in the vicinity of the critical point. It was shown that a thermodynamic potential for the mechanical constitutive equation could be constructed.

In the present work, we have shown that the mechanical potential inherent in the BMP model also corresponds to the thermodynamic potential derived from the model itself, again similar to the Ginzburg–Landau model. We have illustrated that the constitutive equations of the model inherently possess a mechanical potential, which can be identified with the free energy (Eq. (5.2)). Furthermore, it has been shown that the contribution of the normal stresses to the free energy and to the mechanical potential can be evaluated. For values of the second normal-stress difference lower than $0.01\, N_1$, these contributions are not substantial, and the same plateau stress and position of the binodals are obtained.

The construction of the mechanical potential has illustrated the form to build the characteristic curves of the system. In fact, by knowing the parameters u and R, the spinodal, co-existence and bifurcation lines can be defined. This information provides the necessary premises to determine the NECP for the system.

Finally, concerning the elastic instability observed along the high shear-rate branch of the flow curve [22, 23], it is tempting to relate the predicted bifurcation in the high-shear-rate branch to this instability. In fact, the formulation of the BMP model for the first normal stress difference along the high-shear branch of the flow curve, reveals a region of stability (region 5, one root) and a region of three roots (section 6) separated by a bifurcation point. Figure 16 shows the first normal stress difference plotted against the shear rate squared for three temperatures, including the critical isotherm. At the bifurcation point, two of the three roots are equal, and for larger N_1, these roots correspond to three shear rates where two of them have physical meaning: the largest root corresponds to the region where the elastic instability is observed, and the second root roughly corresponds to that along the observed shear-banding region. For increasing shear rates, two values of N_1 are predicted and an apparent jump from the high branch to the low branch is observed at a shear rate located along the negative slope of the low branch, after which a single value of N_1 with increasing shear rates is predicted along the positive slope of the low branch. As shown in Ref. [22], the inclusion of normal stresses does not change substantially the position of the plateau stress nor the minima in the thermodynamic potential. The analysis linking the multi-valued region with the elastic instability is currently under attention in our group.

Funding: The authors acknowledge the financial support from CONACYT (National Council for Science and Technology).

References

[1] R. Miller, Giant micelles: Properties and applications: *AICHE J.* **54** (2008), 3029–3029.
[2] H. Rehage and H. Hoffmann, Shear induced phase transitions in highly dilute aqueous detergent solutions, *Rheologica Acta* **21** (1982), 561–563.
[3] C. Grand, J. Arrault and M. E. Cates, Slow transients and metastability in wormlike micelle rheology, *J. Phys. II France* **7** (1997), 1071–1086.
[4] R. W. Mair and P. T. Callaghan, Observation of shear banding in worm-like micelles by nmr velocity imaging, *Europhys. Lett.* **36** (1996), 719.
[5] C.-Y. D. Lu, P. D. Olmsted and R. C. Ball, Effects of nonlocal stress on the determination of shear banding flow, *Phys. Rev. Lett.* **84** (2000), 642–645.
[6] S. Lerouge, J. P. Decruppe and C. Humbert, Shear banding in a micellar solution under transient flow, *Phys. Rev. Lett.* **81** (1998), 5457–5460.
[7] J.-B. Salmon, A. Colin, S. Manneville and F. M. C. Molino, Velocity profiles in shear-banding wormlike micelles, *Phys. Rev. Lett.* **90** (2003), 228303.
[8] N. A. Spenley, M. E. Cates and T. C. B. McLeish, Nonlinear rheology of wormlike micelles, *Phys. Rev. Lett.* **71** (1993), 939–942.
[9] G. Porte, J.-F. Berret and J. L. Harden, Inhomogeneous flows of complex fluids: Mechanical instability versus non-equilibrium phase transition, *J. Phys. II France* **7** (1997), 459–472.
[10] J.-F. Berret, D. C. Roux and G. Porte, Isotropic-to-nematic transition in wormlike micelles under shear, *J. Phys. II France* **4** (1994), 1261–1279.
[11] J.-F. Berret and G. Porte, Metastable versus unstable transients at the onset of a shear-induced phase transition, *Phys. Rev. E* **60** (1999), 4268–4271.
[12] J. R. A. Pearson, Flow curves with a maximum, *J. Rheology* **38** (1994), 309–331.
[13] P. Olmsted, Perspectives on shear banding in complex fluids, *Rheologica Acta* **47** (2008), 283–300.
[14] R. Podgornik, Book review: Phase transition dynamics, *J. Stat. Phys.* **112** (2003), 429–432.
[15] H. E. Stanley, *Introduction to Phase Transitions and Critical Phenomena*, vol. 1, Oxford University Press, Oxford 1987.
[16] D. Jou, M. Criado-Sancho, L. del Castillo and J. Casas-Vázquez, A thermodynamic model for shear-induced concentration banding and macromolecular separation, *Polymer* **42** (2001), 6239–6245.
[17] D. Jou, J. Casas-Vázquez, M. Criado-Sancho and D. Jou, *Thermodynamics of Fluids Under Flow*, Springer, Berlin, 2001.
[18] O. Manero, J. Pérez-López, J. Escalante, J. Puig and F. Bautista, A thermodynamic approach to rheology of complex fluids: The generalized BMP model, *J. Non-Newton. Fluid* **146** (2007), 22–29.
[19] F. Bautista, J. Soltero, E. Macías, J. Puig and O. Manero, Irreversible thermodynamics approach and modeling of shear-banding flow of wormlike micelles, *J. Phys. Chem. B* **106** (2002), 13018–13026.
[20] D. Jou, J. Casas-Vázquez and G. Lebon, *Extended Irreversible Thermodynamics*, Springer, Berlin, 1996.
[21] K. Sato, X.-F. Yuan and T. Kawakatsu, Why does shear banding behave like first-order phase transitions? Derivation of a potential from a mechanical constitutive model, *Eur. Phys. J. E* **31** (2010), 135–144.
[22] F. Bautista, M. Muñoz, J. Castillo-Tejas, J. H. Pérez-López, J. E. Puig and O. Manero, Critical phenomenon analysis of shear-banding flow in polymer-like micellar solutions. 1. Theoretical approach, *J. Phys. Chem. B* **113** (2009), 16101–16109.

[23] F. Bautista, V. Fernández, E. Macías, J. Pérez-López, J. Escalante, J. Puig and O. Manero, Experimental evidence of the critical phenomenon and shear banding flow in polymer-like micellar solutions, *J. Non-Newton. Fluid* **177–178** (2012), 89–96.

Received October 22, 2014; accepted November 13, 2014.